Eur. Phys. J. E **26**, 169–176 (2008)
DOI 10.1140/epje/i2007-10248-6

THE EUROPEAN PHYSICAL JOURNAL E

Importance of depletion interactions for structure and dynamics of ferrofluids

P. Ilg[a]

ETH Zürich, Department of Materials, Polymer Physics, HCI H541, CH-8093 Zürich, Switzerland

Received 21 September 2007 and Received in final form 16 November 2007
Published online: 20 February 2008 –

Abstract. The influence of attractive depletion forces on the structure and dynamics of ferrofluids is studied by computer simulations. In the presence of a magnetic field, we find that sufficiently strong depletion forces lead to an assembly of particle chains into columnar structures with hexagonal ordering inside the columns. In a planar shear flow, this ordering is destroyed, leading to strong shear thinning behavior. A pronounced anisotropy of the shear viscosity is observed. The viscosity is found to be largest when the magnetic field is oriented in the gradient direction of the flow.

PACS. 75.50.Mm Magnetic liquids – 61.20.Ja Computer simulation of liquid structure – 66.20.Cy Theory and modeling of viscosity and rheological properties, including computer simulations – 83.10.Mj Molecular dynamics, Brownian dynamics

1 Introduction

Dispersions of nano-size ferromagnetic particles —so-called ferrofluids— show strong responses to external magnetic fields [1,2]. In particular their flow behavior can be modified by varying the strength of the applied field [3], which opens several practical applications of these fluids.

Over the last years, the understanding of the flow behavior of ferrofluids has improved significantly due to experimental and theoretical investigations [4]. For dilute ferrofluids with weak dipolar interactions, the viscosity change with varying magnetic-field strength is successfully described by the hindrance of rotation of individual particles [5,6]. Other ferrofluids show a viscosity increase which is much stronger than predicted by the single-particle model [3]. Such a strong viscosity increase can be explained under the assumption that the magnetic particles form chain-like aggregates [7]. This assumption is supported by nonequilibrium simulation results [8–10] as well as by small-angle neutron scattering (SANS) results under shear flow [11].

While equilibrium chain formation in magnetic fluids has been predicted theoretically long ago and has subsequently been studied extensively in the literature (see [12] for a recent review), it came as a surprise when pseudo-crystalline ordering in bulk ferrofluids were observed in SANS and cryo-TEM experiments [13–15]. In thin films, hexagonal order has been observed experimentally already in [16] and later in [17]. The experimental results [13–15] were interpreted in terms of hexagonal particle arrangements in sheets parallel to the magnetic-field direction. Simulation results [18,19] on a perfectly oriented model-ferrofluid showed similar patterns only for much higher concentrations than appropriate for the experimental ferrofluids. Similarly, hexagonally ordered ground states were predicted in [20] only for very high concentrations. For more realistic values of the fluid parameters, computer simulations could so far not reproduce this pseudo-crystalline ordering [12].

Here we show that hexagonal particle arrangements can indeed be observed in computer simulations for realistic model parameters, if one assumes additional, attractive interactions. Such attractive interactions are well known in colloidal systems and result from depletion forces due to free surfactant molecules forming micellar aggregates [21]. We also study the flow behavior of these fluids by nonequilibrium computer simulations.

The outline of this paper is as follows. In Section 2 we introduce the model system studied here as well as the simulation method. The equilibrium properties and structure of this model are presented in Section 3. In Section 4 we explore the dynamical and viscous properties of the model. Finally, some conclusions are offered in Section 5.

2 Model system and simulation method

We study an extension of the model system used in earlier work [10,22,23]. The system consists of a set of N identical, spherical particles of diameter d_{m} with coordinates

[a] e-mail: pilg@mat.ethz.ch

$\boldsymbol{r}_i$ and magnetic dipole moments $\boldsymbol{m}_i = m\boldsymbol{u}_i$, where m denotes the magnitude and $\boldsymbol{u}_i$ the orientation of the dipole.

2.1 Interaction potential

The interaction energy between particles i and j can be written as

$$U_{ij} = \Phi(r_{ij}) + \Phi^{\mathrm{dd}}(\boldsymbol{r}_{ij}, \boldsymbol{m}_i, \boldsymbol{m}_j), \tag{1}$$

where $\boldsymbol{r}_{ij} = \boldsymbol{r}_i - \boldsymbol{r}_j$, $r_{ij} = |\boldsymbol{r}_{ij}|$ is the distance between particles i and j, and $\Phi(r)$ denotes a spherically symmetric potential to be specified below. The dipole-dipole energy Φ^{dd} is given by

$$\Phi^{\mathrm{dd}}(\boldsymbol{r}, \boldsymbol{m}_1, \boldsymbol{m}_2) = \frac{\mu_0}{4\pi}\left[\frac{\boldsymbol{m}_1\cdot\boldsymbol{m}_2}{r^3} - \frac{3(\boldsymbol{m}_1\cdot\boldsymbol{r})(\boldsymbol{m}_2\cdot\boldsymbol{r})}{r^5}\right]. \tag{2}$$

The strength of dipolar interactions relative to the thermal energy is measured by the dipolar interaction parameter λ defined by

$$\lambda = \mu_0 m^2/4\pi k_{\mathrm{B}} T d_{\mathrm{m}}^3. \tag{3}$$

In the presence of a magnetic field $\boldsymbol{H}$, the dipole moment $\boldsymbol{m}_i$ acquires the additional field energy $U_i^H = -\mu_0 \boldsymbol{m}_i\cdot\boldsymbol{H}$. For later use, we introduce the Langevin parameter $\alpha = \mu_0 m|\boldsymbol{H}|/k_{\mathrm{B}}T$, which is a dimensionless measure for the strength of the magnetic field compared to the thermal energy.

The ferrofluids used in the investigations [13–15] are sterically stabilized by a surface layer of surfactant molecules. The resulting, repulsive steric interactions are usually modeled either as truncated Lennard-Jones potential [24] or, slightly more realistic, by the entropic repulsion of interpenetrating surfactant molecules proposed by Rosensweig [9,10]:

$$\Phi^{\mathrm{s}}(r) = \begin{cases} \frac{N_{\mathrm{p}} k_{\mathrm{B}} T}{2\delta}\{\tilde{d_{\mathrm{h}}} + r[\ln(\tilde{d_{\mathrm{h}}}/r) - 1]\}, & \text{for } d_{\mathrm{m}} \le r \le \tilde{d_{\mathrm{h}}} \\ 0, & \text{else.} \end{cases} \tag{4}$$

The number of polymer molecules on the surface and their effective length are denoted by N_{p} and δ, respectively. The quantity $\tilde{d_{\mathrm{h}}} = d_{\mathrm{m}} + 2\delta$ gives the range of the repulsive interaction. Typical values are $N_{\mathrm{p}} \approx 100$–$300$ and $\delta \approx 2\,\mathrm{nm}$. We assume the stabilizing shell to be thick enough, such that van der Waals interaction can be neglected. Ferrofluid models with these interactions have been considered, *e.g.*, in [9,10,23]. See [25] for Brownian-dynamics simulations on electrostatically stabilized ferrofluids.

The spherical potential $\Phi(r)$ in equation (1) contains not only the repulsive potential (4) but also an additional contribution Φ^{dep},

$$\Phi(r) = \Phi^{\mathrm{s}}(r) + \Phi^{\mathrm{dep}}(r), \tag{5}$$

which accounts for an effective attractive interaction between the colloidal particles that is known as depletion interaction [21]. For the functional form of $\Phi^{\mathrm{dep}}(r)$ we employ the approximation proposed by Vrij [21],

$$\Phi^{\mathrm{dep}}(r) = -\Phi^0_{\mathrm{dep}}\left[1 - \frac{3r}{2(\tilde{d_{\mathrm{h}}} + d_{\mathrm{misc}})} + \frac{1}{2}\left(\frac{r}{\tilde{d_{\mathrm{h}}} + d_{\mathrm{misc}}}\right)^3\right], \tag{6}$$

for $\tilde{d_{\mathrm{h}}} \le r \le \tilde{d_{\mathrm{h}}} + d_{\mathrm{misc}}$ and $\Phi_{\mathrm{dep}}(r) = 0$, otherwise. The strength of the depletion interaction can be estimated as $\Phi^0_{\mathrm{dep}} = k_{\mathrm{B}} T \phi_{\mathrm{misc}}(1 + \tilde{d_{\mathrm{h}}}/d_{\mathrm{misc}})^3$ [21]. The diameter and volume fraction of the micelles are denoted by d_{misc} and ϕ_{misc}, respectively.

Adding steric repulsion and depletion interaction, the spherical potential $\Phi(r)$ develops a minimum and the model becomes more similar to a Stockmayer-fluid [26]. The importance of attractive interactions for condensation phenomena has been emphasized frequently in the literature [27,26] and recently also in the context of ferrofluids [28,29]. The influence of depletants on ferrofluid emulsions was studied experimentally in [30,31]. The phase behaviour of ferrofluids containing depletants was studied theoretically and experimentally in [32,33].

2.2 Model dynamics

Two basic mechanisms are known by which the magnetization of a ferrofluid relaxes. First, Brownian rotational motion of the particles leads to a relaxation of the magnetization. The time scale for this process is the rotational relaxation time of a single particle in a solvent with viscosity η_{s}, $\tau_{\mathrm{B}} = \pi\eta_{\mathrm{s}} d_{\mathrm{h}}^3/2k_{\mathrm{B}}T$. Here and in the following, d_{h} denotes the hydrodynamic diameter of the colloidal particles, to be determined below. The second, Néel relaxation mechanism is associated with thermal activation of the internal magnetic moment with respect to the crystallographic axis, $\tau_{\mathrm{N}} \propto \exp[K\pi d_{\mathrm{m}}^3/6k_{\mathrm{B}}T]$, K being the anisotropy constant of the magnetic material. For cobalt, a typical value is $K = 2.5\times10^5\,\mathrm{J/m^3}$ [34]. We consider here particles that are larger than a critical diameter. In this case $\tau_{\mathrm{N}} \gg \tau_{\mathrm{B}}$ and the magnetic moment can be considered as effectively frozen within the particle. This assumption is justified for the fluid used in the experiment [13] with $d_{\mathrm{m}} \approx 8\,\mathrm{nm}$ cobalt particles, since their critical diameter is approximately 5 nm [35].

In the presence of a macroscopic flow field $\boldsymbol{V}(\boldsymbol{r})$ with vorticity $\boldsymbol{\Omega}(\boldsymbol{r}) = (1/2)\nabla_{\boldsymbol{r}}\times\boldsymbol{V}(\boldsymbol{r})$, the Brownian dynamics of the system is described by [8,9,24,10]

$$0 = \boldsymbol{F}_i - \xi_{\mathrm{t}}[\boldsymbol{v}_i - \boldsymbol{V}(\boldsymbol{r})] + \boldsymbol{F}_i^{\mathrm{B}}, \tag{7}$$

$$0 = \boldsymbol{N}_i - \xi_{\mathrm{r}}[\boldsymbol{\omega}_i - \boldsymbol{\Omega}(\boldsymbol{r})] + \boldsymbol{T}_i^{\mathrm{B}}. \tag{8}$$

The velocity and angular velocity of particle i are denoted by $\boldsymbol{v}_i$ and $\boldsymbol{\omega}_i$, respectively. The potential forces and torques are given by $\boldsymbol{F}_i = -\nabla_{\boldsymbol{r}_i} U$ and $\boldsymbol{N}_i = -\boldsymbol{\mathcal{L}}_i U$, respectively, with the rotational operator $\boldsymbol{\mathcal{L}}_i = \boldsymbol{u}_i \times \partial/\partial\boldsymbol{u}_i$. The second terms on the right-hand side of the above equations describe the friction forces and torques. For hard spheres of diameter d_{h}, the translational and rotational friction coefficients are given by $\xi_{\mathrm{t}} = 3\pi\eta_{\mathrm{s}} d_{\mathrm{h}}$ and $\xi_{\mathrm{r}} =$

$\pi\eta_s d_h^3$, respectively. For smooth repulsive short-ranged interactions $\Phi(r)$, a hydrodynamic diameter d_h is defined with the help of the equivalent hard-sphere diameter $d_h = \int_0^\infty dr(1 - \exp[-\beta\Phi(r)])$, $\beta = (k_B T)^{-1}$ as proposed by Barker and Henderson [36]. Since Φ vanishes for $r \geq \tilde{d}_h$, the equivalent hard-sphere diameter is smaller than the range of Rosensweig's repulsive interaction potential $d_h \leq \tilde{d}_h$. The rapidly fluctuating forces and torques $\boldsymbol{F}_i^B$ and $\boldsymbol{T}_i^B$ are modeled as uncorrelated Gaussian white noise obeying $\langle \boldsymbol{F}_i^B(t)\rangle = \langle \boldsymbol{T}_i^B(t)\rangle = \boldsymbol{0}$ and $\langle \boldsymbol{F}_i^B(t)\boldsymbol{F}_j^B(t')\rangle = 2k_B T\xi_t\delta_{ij}\delta(t-t')\boldsymbol{1}$, $\langle \boldsymbol{T}_i^B(t)\boldsymbol{T}_j^B(t')\rangle = 2k_B T\xi_r\delta_{ij}\delta(t-t')\boldsymbol{1}$. We consider the free-draining limit, where hydrodynamic interactions can be neglected [37].

Equations (7) and (8) are obtained in the overdamped limit $M\dot{\boldsymbol{v}}_i \to \boldsymbol{0}$ and $\Theta\dot{\boldsymbol{\omega}}_i \to \boldsymbol{0}$ from the corresponding Langevin equations. M denotes the mass and Θ the moment of inertia of the particles. The overdamped limit is appropriate on the diffusive time scale ($\tau \gg M/\xi_t, \tau \gg \Theta/\xi_r$), where translational and rotational momenta can be assumed to be equilibrated [37]. For typical ferrofluids including the ones studied in [13], $M/\xi_t \approx \Theta/\xi_r \approx 10^{-13}$ s while $\tau_B \approx 10^{-4} \ldots 10^{-5}$ s, and the overdamped limit is an excellent approximation. Furthermore, we treat depletion interactions as instantaneous. This is a valid assumption here, since we restrict ourselves to time scales larger than the diffusion time of the micelles [38].

2.3 Macroscopic variables

The macroscopic magnetization of the system is given by the ensemble average of the individual magnetic moments, $\boldsymbol{M} = M_{sat}\langle \boldsymbol{u}\rangle$, where $M_{sat} = nm$ is the saturation magnetization and $\langle \boldsymbol{u}\rangle = \frac{1}{N}\sum_{j=1}^N \boldsymbol{u}_j$ denotes the average orientation of the magnetic dipoles.

The definition of the pressure tensor in magnetic fluids has been the subject of a number of studies [39,6,40,41]. The orientational motion leads to an antisymmetric contribution to the viscous pressure tensor $\boldsymbol{p}^a$ if the average angular velocity of the particles $\langle \boldsymbol{\omega}\rangle$ does not match the local vorticity of the flow, $\boldsymbol{p}^a = 3\eta_s\phi\,\boldsymbol{\epsilon}\cdot(\langle\boldsymbol{\omega}\rangle - \boldsymbol{\Omega})$ [6]. The total antisymmetric tensor of rank three (Levi-Civita) is denoted by $\boldsymbol{\epsilon}$. Inserting $\boldsymbol{\omega}_i$ from equation (8) and averaging over the particles, one obtains the familiar expression $\boldsymbol{p}^a = \boldsymbol{M}\times\boldsymbol{H}$. Summing the viscous and Maxwell's magnetic pressure tensor, $\mathsf{P}_M = -\boldsymbol{B}\boldsymbol{H} + (\mu_0 H^2/2)\boldsymbol{1}$ with $\boldsymbol{B} = \mu_0(\boldsymbol{H}+\boldsymbol{M})$ [39], the total pressure tensor is found to be symmetric, expressing the conservation of total angular momentum. Using the standard virial expression for the symmetric traceless part, the total viscous pressure tensor is given by [10]

$$\mathsf{P} = p\boldsymbol{1} - \eta_s\boldsymbol{\Gamma} + \frac{1}{V}\sum_{j<k}^{N}\overline{\boldsymbol{r}_{jk}\boldsymbol{F}_{jk}} + \frac{1}{2}(\boldsymbol{M}\boldsymbol{H} - \boldsymbol{H}\boldsymbol{M}), \quad (9)$$

where $\boldsymbol{\Gamma} \equiv \frac{1}{2}[\nabla_{\boldsymbol{r}}\boldsymbol{v} + (\nabla_{\boldsymbol{r}}\boldsymbol{v})^T]$ is the symmetric velocity gradient, $\boldsymbol{F}_{12} = -\nabla_{\boldsymbol{r}_1}U_{12}$ the force on particle 1 due to particle 2, and $\overline{\ldots}$ denotes the symmetric traceless part.

In a planar shear flow, $\boldsymbol{V}(\boldsymbol{r}) = \dot{\gamma}y\boldsymbol{e}^x$, the shear viscosity is defined by $\eta_{yx} = -P_{yx}/\dot{\gamma}$. Note, that no contribution of the Maxwell pressure tensor to the shear stress arises because of the boundary conditions for the magnetic fields $\boldsymbol{H}$ and $\boldsymbol{B}$ (see, *e.g.*, Chapt. 8.12. of [2]). Similar to the Miesowicz viscosities of liquid crystals [27,42,43,22], different viscosity coefficients η_i can be defined if the magnetic field is oriented in flow ($i = 1$), in gradient ($i = 2$), or in the vorticity direction ($i = 3$) of the flow. In addition, a fourth viscosity coefficient is needed to fully characterize the viscous behavior. This coefficient can be chosen as η_4, the viscosity η_{yx} that is measured if the magnetic field is oriented along the bisector of the flow and gradient direction.

2.4 Simulation algorithm

In order to minimize effects due to the finite system size, periodic boundary conditions were employed. The long-range part of the dipolar interactions were treated with the reaction field method beyond a distance r_c, while all interactions are taken into account explicitly below this value. Most simulation results shown are obtained for $r_c = 5d_m$. We verified that the results do not change significantly upon increasing $r_c = 8d_m$ or employing the Ewald method. The nonequilibrium simulations were performed with standard Lees-Edwards periodic boundary conditions [23].

The equations of motion (7) were integrated with a second-order predictor-corrector scheme, while for equations (8) we use a first-order Euler-Maruyama algorithm adapted to conserve exactly the norm of the unit vectors. The integration time step was chosen as $\Delta t = 5\times10^{-4}\tau_B$ for the equilibrium simulations and reduced, depending on the shear rate, down to $\Delta t = 5\times10^{-5}\tau_B$. Results are presented for systems containing $N = 2048$ particles. Some studies for a larger system of $N = 8000$ particles showed no significant differences.

3 Equilibrium structure

We performed equilibrium simulations of the model system by solving equations (7, 8) with the parameters chosen to mimic the experimental situation. For the cobalt-based ferrofluid investigated in [13], the mean particle size was determined to be $d_m = 7.6$ nm, resulting in a dipolar interaction strength of $\lambda \approx 6$. The steric repulsion was modeled by Rosensweig's potential (4) with $N_p = 100, \delta = 0.2d_m$, such that the resulting hydrodynamic diameter correctly accounts for the measured shell thickness of 2 nm. The steric shell prevents the particles from approaching each other closer than roughly d_h, such that the effective dipolar interaction parameter [4] $\lambda^* = \lambda(d_m/d_h)^3 \approx 3$ is significantly reduced. Since the micelles are formed by the free surfactants, their diameter should correspond to the length of the adsorbed molecules. Therefore, the diameter of the micelles was taken as $d_{misc} = 0.2d_m$, which corresponds to $d_{misc} = 1.5$ nm for $d_m = 7.6$ nm. Note, that even

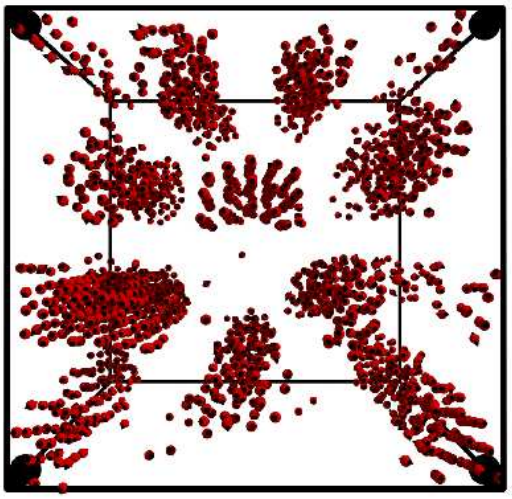

Fig. 1. Snapshot of particle configuration viewed along the magnetic-field direction. The model parameters are $\lambda = 6$, $\phi = 0.06, \phi_{\rm misc} = 0.1, \alpha = 10$.

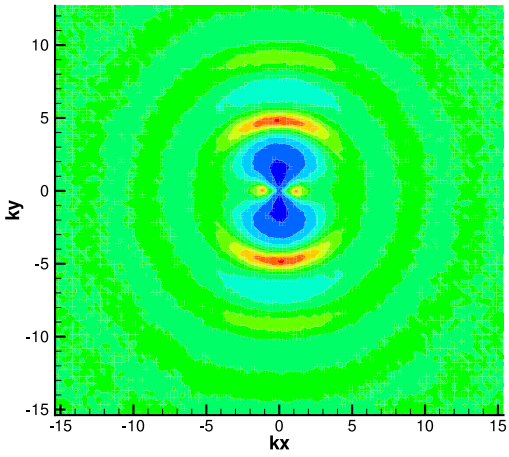

Fig. 2. Static structure factor $S(\boldsymbol{k})$ for the same model parameters as in Figure 1 but for $\phi_{\rm misc} = 0.05$ instead of $\phi_{\rm misc} = 0.01$.

for these size ratios, the pairwise depletion potential has been found to give good predictions on the phase behavior of binary mixtures [44].

Neglecting depletion interactions, $\phi_{\rm misc} = 0$, no sign of hexagonal ordering could be detected in the simulation, for all concentrations investigated $\phi = 0.02 \ldots 0.06$. While the experiments [13] show a pronounced pseudo-crystalline ordering in this regime, the simulations yield only chain-like structures.

However, accounting for sufficient attraction due to depletion interactions, we observe the formation of different equilibrium structures for $\phi_{\rm misc} \gtrsim 0.05$. Figure 1 shows a snapshot configuration viewed along the magnetic-field direction for volume fraction of magnetic particles $\phi = 0.06$, volume fraction of surfactants $\phi_{\rm misc} = 0.1$, Langevin parameter $\alpha = 10$. The formation of columnar structures is obvious.

Figures 2 and 3 show contour plots of the two-dimensional static structure factor $S(\boldsymbol{k}) = \langle \sum_{jk} \exp[i\boldsymbol{k} \cdot \boldsymbol{r}_{jk}] \rangle$ in the plane of the applied field ($\boldsymbol{H}$ in y-direction). The same model parameters as in Figure 1 were chosen. In Figure 2, a scattering pattern typical for chain-like structures is seen, whereas in Figure 3 sharp, distinct peaks at well-defined positions are clearly visible. Both scattering patterns look qualitatively very similar to the experimental ones observed in [13]. In the simulations, the transition from chain-like to more ordered structures occurs at somewhat larger concentrations $\phi \approx 0.04$ compared to the experiments. Another interesting observation from the simulations is that a high concentration of magnetic particles is not necessarily sufficient to cause the transition to the more ordered structures. Indeed, the scattering patterns in Figure 2 are both obtained at the same concentration of magnetic particles $\phi = 0.06$. However, the micellar concentration was chosen as $\phi_{\rm misc} = 0.05$ in Figure 2 and $\phi_{\rm misc} = 0.1$ in Figure 3. This result illustrates the crucial role of attractive depletion interactions for

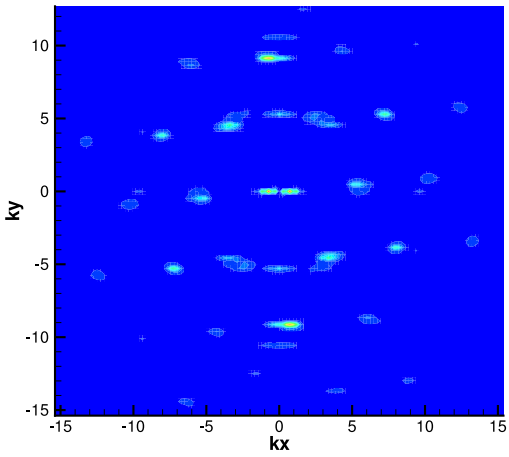

Fig. 3. Static structure factor $S(\boldsymbol{k})$ for the same model parameters as in Figure 1.

structure formation in ferrofluids, at least in the present simulations.

Beyond the qualitative similarities with the experimental results, also the peak positions of Figure 3 are very similar to those in reference [13]. In order to compare the simulation results with the experimental data quantitatively, we follow [13] and calculate $S^\theta(k) = S(\boldsymbol{k} \cdot \boldsymbol{n}^\theta)$ as sector-average of the two-dimensional scattering structure factor $S(\boldsymbol{k})$ of Figure 3 along the unit vector $\boldsymbol{n}^\theta$ in the direction θ. Figure 4 shows a comparison of the experimental curves for $S^\theta(k)$ given in [13] to the simulation results. We observe that the peak positions $k_1 \approx 0.3\,{\rm nm}^{-1}$ and $k_2 \approx 0.57\,{\rm nm}^{-1}$ for $\theta = 0°$ and $30°$ agree nicely between experiment and simulation. For $\theta = 30°$ also the peak height is quantitatively reproduced by the simulations, whereas the peaks in the simulations are smaller than

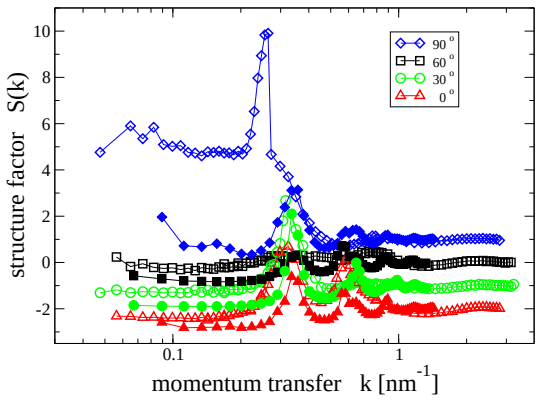

Fig. 4. Sector averages of the static structure factor $S^{\theta}(\boldsymbol{k})$ as a function of k for angles $\theta = 90°, 60°, 30°$, and $0°$. For better visibility the curves are shifted horizontally by $+1, 0, -1$, and -2, respectively. Open symbols denote the experimental values of [13], while solid symbols are the simulation results obtained in this work.

the experimental ones for $\theta = 0°$. The simulations agree with the experimental results also for an angle $\theta = 60°$, where the peak heights are much smaller compared to $\theta = 0°, 30°$. Strong peaks are again observed for $\theta = 90°$, both in experiments and simulations. However, the values for the position and height of the main peak for $\theta = 90°$ differ significantly between experiment and simulation. While in the experiments the main peak is located at $k_3 \approx 0.24\,\mathrm{nm}^{-1}$, the corresponding peak in the simulations is at lower k with much larger height (not shown). The position of this peak in the simulations corresponds to length of the simulation box and is therefore clearly affected by the finite system size. In the experiments, the peak at k_3 is attributed to the spacing between layers of hexagonal ordering [13]. This feature seems to be absent in the simulations. The second peak at k_1, due to hexagonal in-plane ordering is reproduced in the simulations.

Having studied the equilibrium structures of the ferrofluid model, we now proceed to investigate its dynamical properties in a given shear flow.

4 Dynamics in shear flow

It is well known that structural and dynamical properties of complex fluids are intimately related [27,42]. For dilute and chain-forming ferrofluids, a number of experimental and theoretical studies have been performed on this relationship in the last years [11,45,10]. The flow properties of ferrofluids with pseudo-crystalline equilibrium structures as those described in Section 3 are, however, largely unknown. Simulation studies on simple model systems of perfectly oriented ferrofluids show a strong anisotropy of viscous response and strong shear thinning behavior [18]. These features are reminiscent of magnetorheological fluids.

We study the present model in a planar shear flow for a range of shear rates $5 \times 10^{-3} \leq \mathrm{De} \leq 1$, where

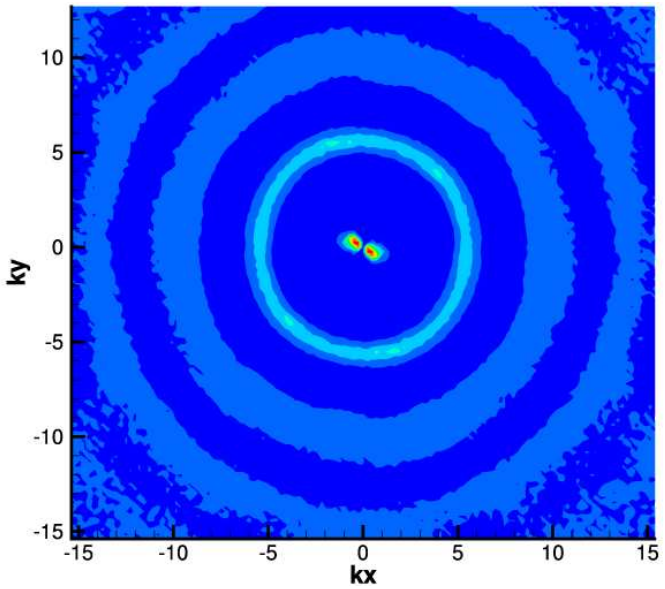

Fig. 5. Static structure factor $S(\boldsymbol{k})$ in planar shear flow with dimensionless shear rate $\mathrm{De} = 0.01$. The magnetic field with strength $\alpha = 10$ is oriented in the gradient direction. The other parameters are chosen as in Figure 1.

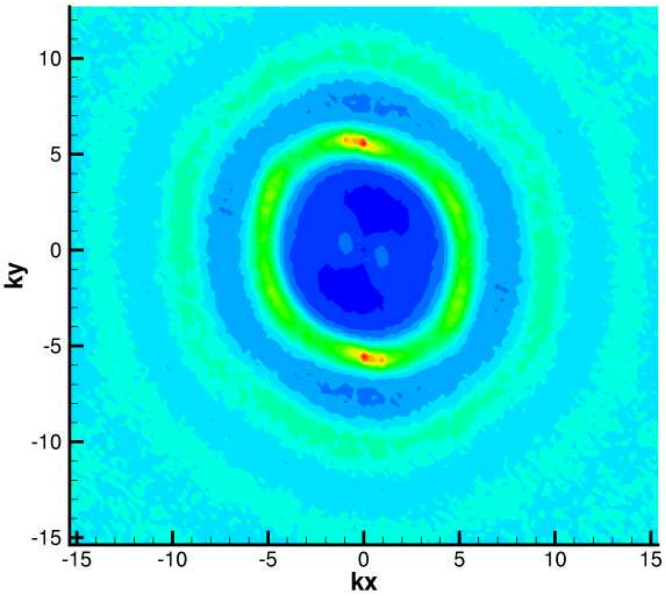

Fig. 6. Same as Figure 5 but for a dimensionless shear rate $\mathrm{De} = 1.0$.

$\mathrm{De} = \tau_{\mathrm{B}}\dot{\gamma}$ is the Deborah number, *i.e.* the shear rate $\dot{\gamma}$ measured in units of inverse Brownian relaxation time. Equations (7) and (8) were integrated numerically until a stationary state was reached. Data were extracted in the stationary state for further time intervals of typically 10^2–$10^3\,\tau_{\mathrm{B}}$. Error bars were estimated from standard deviations of block averages.

Figures 5 and 6 show two-dimensional projections of the static structure factor onto the shear plane for different

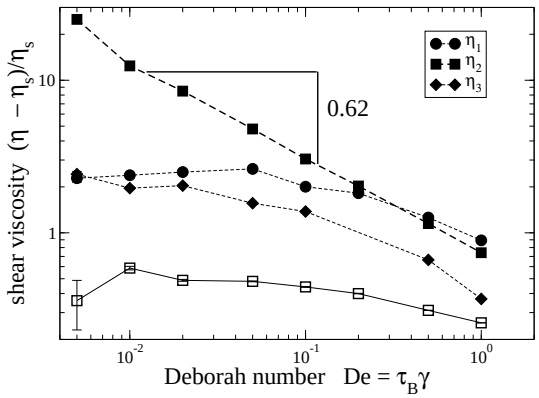

Fig. 7. Relative change of shear viscosity $(\eta_i - \eta_s)/\eta_s$ with respect to solvent viscosity η_s as a function of dimensionless shear rate $\mathrm{De} = \tau_B\dot{\gamma}$, where $i = 1, 2, 3$ corresponds to orientation of the magnetic field in flow, gradient and vorticity direction, respectively. Solid symbols correspond to $\phi_{\mathrm{misc}} = 0.1$, while open symbols $\phi_{\mathrm{misc}} = 0.05$. Otherwise, the same model parameters as in Figure 1 are used.

values of the shear rate. The structure factor clearly shows significant structural changes due to the applied flow. The distinct peaks in equilibrium seen in Figure 3 get washed out by the shear flow. We note that the lowest shear rate studied $\mathrm{De} = 5 \times 10^{-3}$ is already strong enough to destroy the hexagonal equilibrium ordering in case the field is oriented along the gradient direction of the flow. For increasing shear rate, also the peak at the lowest wave vector k disappears. Instead, shear-induced anisotropy of local particle arrangements is seen at high shear rates, Figure 6, similar to earlier observations [42,18].

The strong structural changes are reflected in the shear thinning behavior shown in Figure 7. The viscosity coefficient η_2 corresponds to the magnetic field being oriented along the gradient direction of the flow. This geometry was also used in Figures 5 and 6. A strong shear-thinning behavior is apparent from Figure 7 with a power law behavior $\eta_2 \propto \dot{\gamma}^{-\nu}$. The shear-thinning exponent $\nu \approx 0.6$ observed here is slightly higher than 1/2 which can be estimated from the force balance on a chain of ferromagnetic particles [35]. On the other hand, the exponent ν found here is smaller than $\nu = 1$ which is the typical value for magnetorheological fluids (see, *e.g.*, G. Bossis *et al.* in [1,42]). For a two-dimensional model system, an exponent $\nu = 0.75$ was found in [9] for a higher concentration and at much higher dipolar interaction strengths.

For different orientations of the magnetic field with respect to the flow geometry, the viscosity coefficients differ considerably. If the magnetic field is oriented parallel to the flow direction, the corresponding viscosity coefficient η_1 is much lower than η_2, since in this case the extended structures provide less resistance to the flow. Furthermore, the plateau of η_1 for decreasing shear rate $\dot{\gamma}$ indicates that the low shear rate regime has been reached for this quantity. Finally, orienting the magnetic field parallel to the vorticity direction, *i.e.* perpendicular to the shear plane, gives the smallest viscosity value η_3. The observed ordering of the viscosity coefficients $\eta_3 < \eta_1 < \eta_2$ is typical for suspensions of elongated objects [42]. For dimensionless shear rates $\mathrm{De} \gtrsim 0.2$, the values of the viscosity coefficients η_1 and η_2 become quite similar. We conclude therefore that in this regime the particle aggregates are destroyed to a large extent.

From Figure 7 we also observe that the shear viscosity η_2 is significantly larger for $\phi_{\mathrm{misc}} = 0.1$ (solid squares) than for $\phi_{\mathrm{misc}} = 0.05$ (open squares). Therefore, the difference in the equilibrium structures Figures 2 and 3 leaves a trace in the nonlinear viscosity behavior, even though these structures are strongly distorted by the shear flow. Therefore, depletion interactions play an important role also for dynamical properties of ferrofluids.

We verified by a direct cluster analysis [10] of the nonequilibrium particle configurations that the mean cluster size is decreasing significantly due to the shear flow. These results support the intuitive arguments of "chain rupture" being responsible for strong shear thinning behavior in ferrofluids [3].

The viscoelastic behavior of ferrofluids shows up not only in shear-thinning behavior but also in normal stress differences [4]. In agreement with experimental results [4], the first normal stress difference $N_1 = P_{yy} - P_{xx}$ is found to be positive and increasing quadratically with applied field strength for small α if the magnetic field is oriented in the gradient direction. For large α, N_1 is found to saturate to a finite value. The second normal stress difference $N_2 = P_{zz} - P_{yy}$ is found to be negative with $-N_2/N_1 \approx 0.5$. Experimentally, so far there is only a single data point for one value of the magnetic field where $-N_2/N_1 \approx 1/4$ was found in [4] for a magnetite ferrofluid. The results on normal stress differences are consistent with earlier simulation results [23] and with predictions of a dynamical mean-field theory [46].

5 Conclusions

We have performed equilibrium and nonequilibrium computer simulations of realistic model-ferrofluids. In accordance with analytical predictions, and also in agreement with previous studies [9,24], we observe the formation of chain-like equilibrium structures in a magnetic field for a wide range of model parameters. One main new result of the present study is that sufficiently strong depletion forces lead to an assembly of particle chains into columnar structures along the magnetic-field direction. Inside the columns and parallel to the field direction, particles are arranged hexagonally. The corresponding static structure factor agrees well with results from SANS experiments [13] which exhibit very similar characteristic scattering patterns. The experimental results [13] have been interpreted in terms of hexagonal ordering in sheets parallel to the field direction. The present simulations indeed show such a hexagonal ordering within columnar structures. The present study therefore suggests that attractive interactions due to depletion forces lead to these ordered structures. The observations that hexagonal ordering has so far been found only in some ferrofluids, can

then be explained naturally by the different amounts of free surfactant present in these fluids. Indeed it was mentioned in [13] that "additional surfactants have been used in excess" in some of the fluids studied. Unfortunately, the precise amount of free surfactants in these fluids remains unclear. Some quantitative discrepancies between simulation and experimental results can probably be attributed to finite-size effects. However, we cannot exclude that these discrepancies indicate some differences between the observed structures. This point deserves further studies. In any case, the present study clearly demonstrates the importance of depletion forces for the structure formation in ferrofluids. While the crucial role of depletion forces is well known in ordinary colloidal suspensions, apparently so far it has not been appreciated enough for ferrofluids.

Beyond studying (and to a large extend reproducing the experimental results on) the static structure, we also explored the flow behavior of these model-ferrofluids. We find a strong anisotropy of the viscous behavior with the shear viscosity being largest when the magnetic field is oriented along the gradient direction of the flow. This behavior is characteristic for the rheology of suspensions of elongated objects. Furthermore, we observe a strong shear thinning behavior if the field is oriented in gradient direction of the flow.

Due to computational limitations, we have so far not reached the Newtonian, low shear rate regime if the magnetic field is oriented in the gradient direction of the flow. The same problems appears generally in nonequilibrium simulations: in order to reach the stationary state for a given shear rate $\dot{\gamma}$, the simulations must span time intervals $t \gg 1/\dot{\gamma}$ which soon exceed the available computing times. Thus, already for the lowest shear rates studied, the equilibrium structures are severely distorted and we do not detect any characteristic difference to the rheology of other chain-forming ferrofluids. Since $\tau_B = 10^{-4}$–10^{-5} s for typical ferrofluids, the lowest shear rate studied here $\mathrm{De} = \tau_B\dot{\gamma} = 5 \times 10^{-3}$ still corresponds to a laboratory shear rate $\dot{\gamma} = 50$–$10^3\,\mathrm{s}^{-1}$. For the cobalt fluid in [13] with the low viscous solvent toluene, the relaxation time τ_B is even shorter. Therefore, we suggest an experimental investigation of the shear viscosities η_i to be compared to Figure 7 for a ferrofluid containing a high viscous solvent that shows hexagonal equilibrium structures.

I am very grateful for numerous enlightening discussions on this subject with S. Hess, M. Kröger, and A. Wiedenmann. Many thanks to A. Wiedenmann also for providing the experimental data in Figure 4.

References

1. S. Odenbach (Editor), *Ferrofluids. Magnetically Controllable Fluids and Their Applications*, Lect. Notes Phys., Vol. **594** (Springer, Berlin, 2002).
2. R.E. Rosensweig, *Ferrohydrodynamics* (Cambridge University Press, Cambridge, 1985).
3. S. Odenbach, J. Phys.: Condens. Matter **15**, S1497 (2003).
4. S. Odenbach, J. Phys.: Condens. Matter **16**, R1135 (2004).
5. M.I. Shliomis, Sov. Phys. JETP **34**, 1291 (1972).
6. M.I. Shliomis, in *Ferrofluids. Magnetically Controllable Fluids and Their Applications*, edited by S. Odenbach, Lect. Notes Phys., Vol. **594** (Springer, Berlin, 2002) pp. 85–111.
7. A.Y. Zubarev, J. Fleischer, S. Odenbach, Physica A **358**, 475 (2005).
8. A. Satoh, R.W. Chantrell, G.N. Coverdale, J. Colloid Interface Sci. **209**, 44 (1999).
9. H. Morimoto, T. Maekawa, J. Phys. A, Math. Gen. **33**, 247 (2000).
10. P. Ilg, E. Coquelle, S. Hess, J. Phys.: Condens. Matter **18**, S2757 (2006).
11. L.M. Pop, S. Odenbach, J. Phys.: Condens. Matter **18**, S2785 (2006).
12. C. Holm, J.J. Weis, Curr. Opin. Colloid Interface Sci. **10**, 133 (2005).
13. A. Wiedenmann, A. Hoell, M. Kammel, P. Boesecke, Phys. Rev. E **68**, 031203 (2003).
14. M. Klokkenburg, B.H. Erné, J.D. Meeldijk, A. Wiedenmann, A.V. Petukhov, R.P.A. Dullens, A.P. Philipse, Phys. Rev. Lett. **97**, 185702 (2006).
15. M. Klokkenburg, B.H. Erné, A. Wiedenmann, A.V. Petukhov, A.P. Philipse, Phys. Rev. E **75**, 051408 (2007).
16. C.Y. Hong, I.J. Jang, H.E. Horng, C.J. Hsu, Y.D. Yao, H.C. Yang, J. Appl. Phys. **81**, 4275 (1997).
17. A. Yethiraj, A. van Blaaderen, Nature **421**, 513 (2003).
18. S. Hess, T. Weider, M. Kröger, Magnetohydrodynamics **37**, 297 (2001).
19. S. Hess, in *Physics of Complex and Supramolecular Fluids*, edited by S.A. Safran, N.A. Clark (Wiley-Interscience, New York, 1987) pp. 631–642.
20. B. Groh, S. Dietrich, Phys. Rev. E **63**, 021203 (2001).
21. A. Vrij, Pure Appl. Chem. **48**, 471 (1976).
22. P. Ilg, M. Kröger, S. Hess, Phys. Rev. E **71**, 051201 (2005).
23. P. Ilg, M. Kröger, S. Hess, Phys. Rev. E **71**, 031205 (2005).
24. Z. Wang, C. Holm, H.W. Müller, Phys. Rev. E **66**, 021405 (2002).
25. G. Mériguet, M. Jardat, P. Turq, J. Chem. Phys. **123**, 144915 (2005).
26. L.L. Lee, *Molecular Thermodynamics of Nonideal Fluids* (Butterworth-Heinemann, 1988).
27. R.G. Larson, *The Structure and Rheology of Complex Fluids* (Oxford University Press, New York, 1999).
28. Y. Lalatonne, J. Richardi, M.P. Pileni, Nature Mater. **3**, 121 (2004).
29. E.M. Claesson, A.P. Philipse, Langmuir **21**, 9412 (2005).
30. J. Bibette, J. Magn. & Magn. Mater. **122**, 37 (1993).
31. M. Ivey, J. Liu, Y. Zhu, S. Cutillas, Phys. Rev. E **63**, 011403 (2000).
32. G.A. van Ewijk, G.J. Vroege, Langmuir **18**, 377 (2002).
33. G.A. van Ewijk, G.J. Vroege, B.W.M. Kuipers, Langmuir **18**, 382 (2002).
34. M. Jamet, W. Wernsdorfer, C. Thirion, D. Mailly, V. Dupuis, P. Mélinon, A. Pérez, Phys. Rev. Lett. **86**, 4676 (2001).
35. S. Odenbach, *Magnetoviscous Effects in Ferrofluids*, Lect. Notes Phys., Vol. **71** (Springer, Berlin, 2002).
36. J.A. Barker, D. Henderson, J. Chem. Phys. **47**, 4714 (1976).
37. J.K.G. Dhont, *An introduction to dynamics of colloids*, Stud. Interface Sci. (Elsevier, Amsterdam, 1996).

38. G.A. Vliegenthart, P. van der Schoot, Europhys. Lett. **62**, 600 (2003).
39. B.U. Felderhof, Phys. Rev. E **62**, 3848 (2000).
40. C. Rinaldi, H. Brenner, Phys. Rev. E **65**, 036615 (2002).
41. M. Liu, K. Stierstadt, arXiv:cond-mat/0010261 (2000).
42. S. Hess, in *Advances in the Computer Simulation of Liquid-Crystals*, edited by P. Parisi, C. Zannoni (Kluwer, Dordrecht, 2000) pp. 189–233.
43. M. Kröger, P. Ilg, S. Hess, J. Phys.: Condens. Matter **15**, S1403 (2003).
44. M. Dijkstra, R. van Roij, R. Evans, Phys. Rev. Lett. **82**, 117 (1999).
45. A.Y. Zubarev, L.Y. Iskakova, Phys. Rev. E **61**, 5415 (2000).
46. P. Ilg, S. Hess, Z. Naturforsch. **58a**, 589 (2003).